



Automatic three-dimensional imaging for blastomere identification in early-stage embryos based on brightfield microscopy

Sheng Yao^{a,b}, James K. Mills^{b,*}, Ihab Abu Ajamieh^b, Hai Li^a, Xianmin Zhang^{a,*}

^a Guangdong Key Laboratory of Precision Equipment and Manufacturing Technology, School of Mechanical and Automotive Engineering, South China University of Technology, Guangzhou, 510640, China

^b Department of Mechanical and Industrial Engineering, University of Toronto, Toronto, M5S 3G8, Canada

ARTICLE INFO

Keywords:

3D imaging technique
Brightfield microscopy
Depth from focus
Automated preimplantation genetic diagnosis
Blastomere localization

ABSTRACT

As the first step in manual or automated preimplantation genetic diagnosis (PGD), accurate locating of the blastomere is essential. In order to further improve success rates of the PGD process, it is necessary to obtain three-dimensional information of the blastomeres. In this study, a practical and effective pipeline that allows conventional brightfield microscopy systems to provide 3D imaging feedback for individual blastomeres inside embryos is proposed. The technique consists of two main phases, namely the blastomere identification and the 3D modeling of individual blastomeres. In the first phase, after a series of optical sections are obtained along the z-axis (z-stack), the embryo is located in the z-stack and the blastomere outline is then identified inside the embryo using a coarse-to-fine strategy; In the second phase, a probabilistic model combined with the machine learning approach is designed for the boundary estimation between individual blastomeres, and the 3D coordinate and model of each blastomere are obtained through further relocalization and reconstruction in the z-stack. Experimental results demonstrate that the proposed technique is valid and accurate compared with human perception. Specifically, the proposed technique achieves 90.32% precision rate, and the bias of blastomere position between the proposed method and human segmentation is 1.028 μm .

1. Introduction

In the past decades, assisted reproductive technology (ART) has become the predominant treatment for infertility [1]. As a core process in ART, in vitro fertilization (IVF) focuses on delicate manipulation of early-development-stage embryos. In order to avoid certain diseases or disorders, preimplantation genetic diagnosis (PGD) is usually required in the IVF [2], i.e., extracting a blastomere from the early-stage embryo for genetic analysis (which is known as embryo biopsy). Up to date, embryo biopsy is normally performed by proficient operators that requires years of training. Nevertheless, the corresponding clinical pregnancy rate is only 23.3% according to the data in the latest two years [3]. To increase the clinical pregnancy rate, one promising solution is to automate the PGD process by using robotic systems since it can eliminate potential contamination and improve manipulation accuracy [4].

As one of the crucial step in the PGD process, blastomere extraction involves removal of a single blastomere from the embryo without damaging the blastomere or the embryo itself. To automate the PGD process utilizing robotics, effective identification and location of the blastomeres based on image processing technique is indispensable. Recently, various imaging techniques have been adopted in the community of automated

cell manipulation. For instance, Wong et al. [5] optimize the membrane drilling location by using texture-based segmentation. In Ref[6], Ang et al. demonstrate the use of edge detection for the location of dissection. Although many different methods have been proposed, most of them locate the blastomere in one plane. Since blastomeres exist in 3D space and may have irregular shapes, it would be very meaningful if 3D information of the blastomeres can be obtained during the manipulation process.

3D information is beneficial to increase the success rate of cell surgery. Sun et al. develop a robot-aided microscopy system for intracellular surgery [7] and a 3D reconstruction method based on deconvolution and volume rendering for mitochondria extraction [8], which significantly increase the survival rate of organelles. Nowadays, several kinds of 3D optical sectioning technologies are available from the market, such as magnetic resonance imaging (MRI), computer tomography (CT), confocal microscopy. However, MRI and CT are often used to visualize large specimens, such as tissues and organs [9]. Confocal microscopy has several limitations for building robotic manipulation systems, such as high costs of purchase as well as operations of the microscopes, and small workspace for cell surgery. As a commonly used setup in many robotic manipulation systems [10,11], brightfield microscopy

* Corresponding authors.

E-mail addresses: syao@mie.utoronto.ca (S. Yao), mills@mie.utoronto.ca (J.K. Mills), zhangxm@scut.edu.cn (X. Zhang).

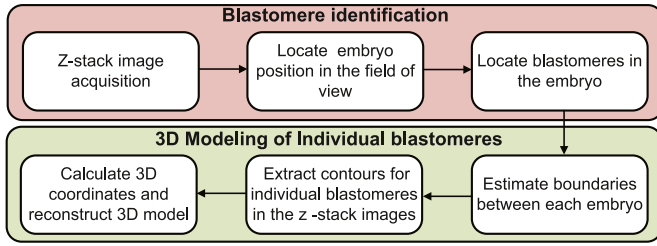


Fig. 1. Pipeline of 3D blastomere imaging under standard brightfield microscopy.

is a practical and suitable setup for 3D imaging [12]. To obtain 3D information from brightfield microscopy, it normally requires a set of 2D planar images taken at uniformly spaced focal planes (z-stack). Although the z-stack of images from conventional brightfield microscopy have been used for the study of entire cell segmentation and reconstruction [13,14], few published literature has presented 3D blastomere imaging techniques with the z-stack. Giusti et al. [15] use a graph-cut based method for blastomere morphology measurements. Nevertheless, this method assumes the blastomeres have a spherical shape and the region of interest for segmentation process is set manually through experiments.

In the z-stack images of embryos, transparent embryos together with their substructures have a complex appearance, which is often considered as an obstruction to automatic processing. Additionally, blastomeres have a thick 3D topology overlap and deform with each other while being affected by varying defocus in the images [16]. Due to such complexity, it remains a challenging task to locate 3D blastomeres separately inside embryos through the brightfield microscopes. In this paper, a 3D imaging technique to automatically identify and locate blastomeres in early-stage embryos for PGD under brightfield microscopy is developed. The novelty in the proposed method is in the automatic pipeline that combines a series of existing state-of-the-art image processing algorithms with the depth from focus technique to deal with the highly challenging problem. After z-stack images are acquired with a brightfield microscope, the embryo localization in the z-stack is conducted, and a two-step method is introduced to locate the blastomere edge contours within the embryo. To identify the boundaries among individual blastomeres, a method that combines a probabilistic model and linear regression is proposed, and each blastomere is relocated by contour extraction of out-of-focus images. Then, the 3D position of each blastomere is obtained, and the 3D reconstruction is presented. Finally, experiments are performed with embryos to demonstrate the feasibility and effectiveness of the proposed technique. The overview of the pipeline is illustrated in Fig. 1. The proposed 3D imaging technique can greatly benefit embryo biopsy with 3D position information, and facilitate automated embryo image analysis as well as precise vision-based control [34] during embryo manipulation. Specifically, the global optimization of embryo dissection [5] can be enabled based on the proposed technique.

The remainder of the paper is organized as follows. In Section 2.1, the imaging system description and image acquisition principle are introduced. The embryo localization method is addressed in Section 2.2. The localization of blastomeres in the embryo is presented in Section 2.3. Section 2.4 details the estimation of blastomere boundary. Identification and 3D modeling of individual blastomeres are described in Section 2.5. The validity of the proposed method is then verified by experiments in Section 3. Conclusions are given in Section 4.

2. Methodology

2.1. Systems description and image acquisition guideline

The basic concept of embryo z-stack image acquisition under inverted brightfield microscopy for 3D blastomere identification is pre-

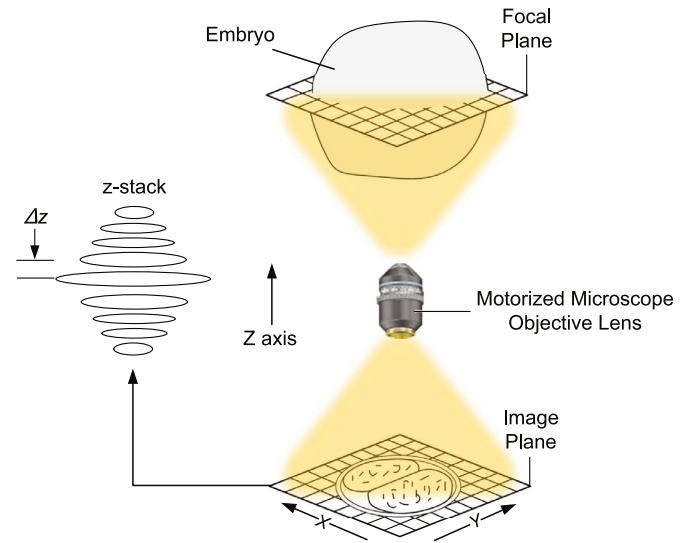


Fig. 2. Acquisition of optical sections based on brightfield microscopy.

sented with a schematic diagram shown in Fig. 2. The microscope objective lens is driven by the focus motor along the z axis direction with a step size Δz , so that the whole embryo is imaged from the bottom to the top. Since the average diameter of a mouse embryo is $70\mu\text{m}$ [17], the length of the z-stack can be safely set as $100\mu\text{m}$. For each optical section in the embryo, an image is captured by the camera correspondingly and subsequently stored. The Depth of Field (DOF) [18] of the microscope can be calculated as:

$$DOF = \frac{\lambda \cdot n_i}{NA^2} + \frac{n_i}{M \cdot NA} r \quad (1)$$

where λ is the illuminating light wavelength of brightfield microscopy, n_i is the refractive index of the medium between the coverslip and the front lens element of the objective lens, and NA represents the objective numerical aperture, r is the smallest resolving distance of the sensor on the image plane, M is the total magnification. In order to fully acquire information of the 3D structure, Δz of the z-stack should be smaller than the DOF of the microscope setup. Once Δz is selected, and number of images is confirmed and z-stack images can be automatically obtained with the motorized focus.

2.2. Automatic localization of embryos

After the z-stack is acquired, embryo localization is conducted in the z-stack by estimating the most in-focus optical section for the embryo and then locating the embryo in the field of view.

Many images in the z-stack contain defocus blurs that make it difficult to distinguish embryos from the background. The images which have good embryo textures are always those with high focus level. To identify a suitable image in the z-stack for embryo localization, global focus assessment is required to estimate the focus level of each image in the z-stack. The Tenengrad variance operator [19] utilizes the variance of the image gradient as the focus measurement, which can be formulated as

$$\phi_{x,y} = \sum_{i,j \in \Omega(x,y)} (G(i,j) - \bar{G})^2 \quad (2)$$

where x and y are image coordinates, $\Omega(x, y)$ is the local neighborhood for each pixel, \bar{G} is the mean value of gradient magnitude, and $G(i, j)$ is the pixel's value of gradient magnitude, which is calculated as $G(i, j) = \sqrt{G_x(i, j)^2 + G_y(i, j)^2}$. Tenengrad variance also shows high robustness to noise and excellent overall performance [20]. Therefore, it is selected as the focus measure operator to evaluate the z-stack image, and the image with the highest focus level values is chosen.

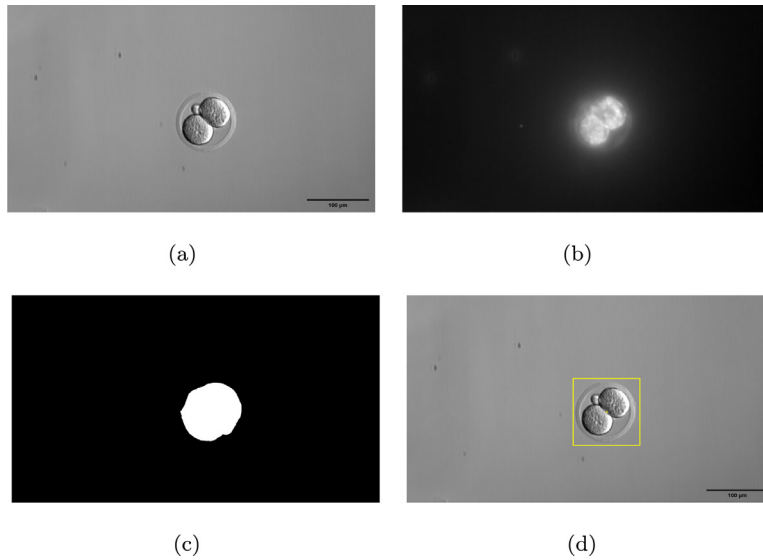


Fig. 3. Visualization of the Gabor feature sets and localization of the embryo in the field of view. (a) High focus level image from the z-stack using Tenengrad variance operator. (b) Visualization of the Gabor feature sets. (c) Post-processing using Otsu's method to obtain the region of interest. (d) Final result.

Further, Gabor filters [21] are utilized to separate the embryo in the field of view. As a reasonable model of cells in the human visual system, Gabor filters are considered to be the model of how humans recognize texture. The two-dimensional Gabor filters are constructed by

$$\begin{cases} h(x, y) = \exp\left(-\frac{1}{2}\left[\frac{x^2}{\sigma_x^2} + \frac{y^2}{\sigma_y^2}\right]\right) \cos(2\pi\mu_0 x) \\ \mu_0 = 1\sqrt{2}, 2\sqrt{2}, 4\sqrt{2}, \dots, (N_c/4)\sqrt{2} \\ \theta_0 = 0^\circ, 45^\circ, 90^\circ, 135^\circ \end{cases} \quad (3)$$

where σ_x and σ_y are the space constants of the Gaussian envelope along the x -axis and y -axis, respectively, μ_0 are sinusoidal plane wave frequencies along the x -axis, N_c is pixel number of the width of the image. θ_0 are the Gabor filter orientations that rotating the $x - y$ spatial system.

After extracting the Gabor energy from the image, Gaussian smoothing is conducted to compensate for the variations of Gabor magnitude features, and principal component analysis [22] is conducted to reshape the Gabor feature sets into an intensity value for each pixel, as shown in Fig. 3(b). It can be seen that there is a sufficient variance in the Gabor feature information between the embryo and the image background due to the texture differences. Then, post-processing using Otsu's method [23] is conducted to automatically locate the embryo position in the field of view, and the region of interest is obtained, as illustrated with a yellow box in Fig. 3(d).

2.3. Identification and localization of blastomeres

Once the embryo is located, the blastomeres are then identified inside the region of interest. Inspired by [8], to obtain high quality images, the noise and defocus blurs can be removed by deconvolution. Thus, the Richardson-Lucy deconvolution algorithm with total-variation regularization (RLTV) [24] is employed. From the signal processing perspective, the image acquisition is considered as the convolution of the light signal X in the observed volume Y with the point spread function (PSF) H , combined with noise degradation N .

$$Y = HX + N \quad (4)$$

Therefore, deconvolution inverts the process of noise convolution in Eq. (4), and improves the contrast and resolution of images captured with the microscopes. The RLTV deconvolution method is a maximum-likelihood approach with a regularization term to eliminate the effect of noise amplification, which can be written as follows, minimizing the cost function:

$$J(X) = \mathbf{1}^T HX - Y^T \log(HX) + \lambda \|DX\|_1 \quad (5)$$

where the log operation is conducted componentwise $\mathbf{1} = (1, \dots, 1) \in \mathbb{N}^N$, λ is a regularization parameter, and D is the finite difference matrix of the first derivative. A precise and efficient approximation of the Gibson-Lanni model [25] is constructed as the 3D PSF H . Then, the region of interest of the z-stack Y is deconvolved based on Eq. (5), and the possessed sections X are obtained for subsequent steps.

A coarse-to-fine method is then designed for blastomere identification inside the embryo. A region-based active contour algorithm is first implemented for the coarse segmentation. An active contour is a deformable curve defined as $c(s) = (x(s), y(s))$, where $s \in [0, 1]$, and x, y are image coordinates. In the spatial domain, the evolution of active contour of an image can turn into minimizing the energy function:

$$E = E_{in}(c) + E_{out}(c) = \int_{in(c)} |I(x, y) - c_i|^2 dx dy + \int_{out(c)} |I(x, y) - c_o|^2 dx dy \quad (6)$$

where E_{in} is the internal energy term, E_{out} is the external energy term, c_i and c_o denote the average pixel values inside and outside the deformable curve c , $I(x, y)$ is the pixel value at image coordinates (x, y) . According to the image energy distribution, the minimization process of the energy function E drives the curve to approach the boundary of the object [26]. The technique that localizes the energy from its global counterpart is also adopted to improve the accuracy and robustness of segmentation [27]. A texture-based thresholding process is used to generate a mask as the initialization of the active contour model. Local standard deviation filtering and binary thresholding are performed. After image closing, the largest connected component is selected as the initial curve of the active contour model. Then, driven by the internal and external forces, the contour is evolved in the embryo image, and the outline of blastomeres is obtained.

With the completion of the aforementioned coarse locating step, fine segmentation adjustment updates the accuracy of blastomere boundary to the subpixel level. The fine segmentation process is performed based on an edge localization algorithm based on the edge and partial region effect acquisition model [28]. Instead of analyzing maximum gradients, the detector assumes the edges from the discontinuity in the image. This technique is suitable for blurred edges with a precision that can reach 0.01 pixel. Both position and orientation of edges are precisely detected. Nevertheless, the complex textures inside the embryos cause many pseudo-edges that do not belong to the blastomere boundary. Thus, a strategy is applied such that only the detected edges within 3 pixels from the coarse segmentation outline are selected and replace the previous ones. Then, the fine localization of blastomeres is achieved, as demonstrated in the green line in Fig. 4. As presented in the zoom-in sub-figure of Fig. 4, the fine blastomere identification in green is more

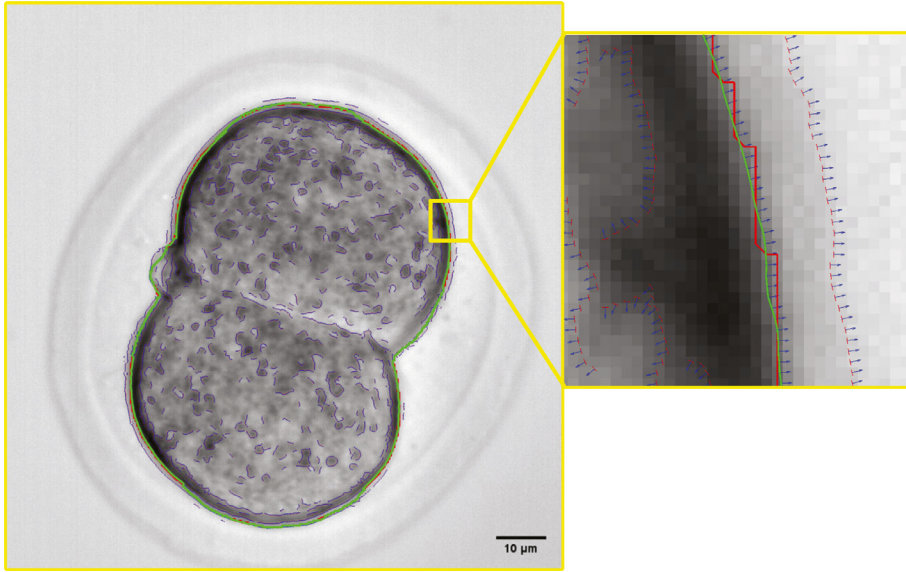


Fig. 4. Coarse-to-fine segmentation of blastomeres inside the embryo. Red line denotes the result of coarse localization. Blue lines are the outputs of the edge detector. Green line denotes the final segmentation.

accurate and much smoother than the coarse identification in red, which shows the capability of the coarse-to-fine method.

2.4. Boundary estimation between each individual blastomere

In the most in-focus optical section of the embryo, the complex textures and low contrast on blastomeres still make it difficult for a computer to distinguish the thin boundary between each blastomere. Many edge detectors either fail to detect the boundary or mix the boundary with heterogeneous textures. Therefore, instead of elementary features such as edges, higher level features such as geometric structures need to be considered. Several principles of visual perception such as good continuation and connectedness can be utilized.

A *contrario* is a probabilistic approach for determining potential good feature continuation in terms of human visual perception. The number of false alarms [29] is defined as the stochastic expectation of an event, which is denoted as

$$N(e) = N_{tests} P_{H_0} \quad (7)$$

where e indicates the event of interest, H_0 is the *a contrario* model, N_{tests} denotes the number of possible occurrences of e , P_{H_0} represents the probability of e happening under H_0 . If $N(e) \leq \epsilon$, the event e will be regarded as ϵ -meaningful. For line segment events, ρ and θ are assumed as the maximum distance and angle between line segments that qualify for good continuation, and n_0 is denoted as the number of different pairs of ρ and θ values. Then, N_{tests} can be regarded as all possible sequences of k line segments in the image out of overall n line segments:

$$N_{tests} = n_0 \cdot \frac{n!}{(n-k)!} \quad (8)$$

In the image domain with width w and length l , the probability that the tip of the second line segment falls into the good continuation area around the tip of the first segment is denoted as $\Pi_\rho \approx \frac{\rho^2 \theta}{wl}$, and the probability of the maximum tolerant angle θ between these two segments is $\Pi_\theta \approx \frac{\theta}{\pi}$. Thus, the probability term $P_{H_0}^{(2)}$ can be expressed as

$$P_{H_0}^{(2)} = \Pi_\rho \Pi_\theta = \frac{(\rho\theta)^2}{\pi wl} \quad (9)$$

Therefore, for a candidate boundary that has the chain of k line segments, there are $k-1$ junctions in total, and its probability $P_{H_0}^{(k-1)} = (\Pi_\rho \Pi_\theta)^{(k-1)}$ is obtained. According to Eq. (7), we can approximate the number of false alarms associated with the event of good continuation

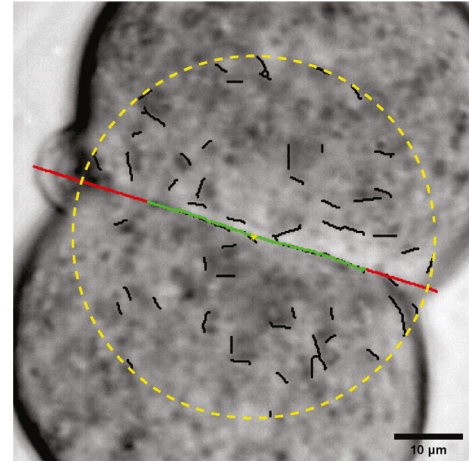


Fig. 5. Estimation of the boundary between individual blastomeres. The yellow dashed circle indicated the region of interest for detecting the boundary. The black lines indicate all initial segments. The green line is the final result using the *a contrario* model, and the red segments are the result from machine learning. (For interpretation of the references to colour in this figure legend, the reader is referred to the web version of this article.)

as

$$N(\rho, \theta, k) = n_0 \cdot \frac{n!}{(n-k)!} \cdot \left(\frac{(\rho\theta)^2}{\pi wl} \right)^{k-1} \quad (10)$$

After the outline of all blastomeres is obtained, the centroid is calculated. Using the shortest distance between the centroid and the outline as the radius, a circular region of interest inside blastomeres is acquired for boundary detection, as shown in the yellow dashed circle in Fig. 5. An automatic line segment detector [30] is exploited to extract the all initial line segments specifically in this circular region of interest, which are marked in black. By fixing $\epsilon = 1$, such that at most only one false detection is accepted for each z-stack image in the *a contrario* model. While θ determines how the smoothness of blastomere boundaries should be, ρ restricts the maximum distances between each line segments in the candidates boundaries, which is proportional to the size of region of interest. Thus, it is acceptable to set $\theta = 60^\circ$ and $\rho = 30$ pixels since two segments of the boundary between individual blastomeres would not dramatically change. After the *a contrario* model is calculated and valid continuation segments are produced, the longest chain is selected as

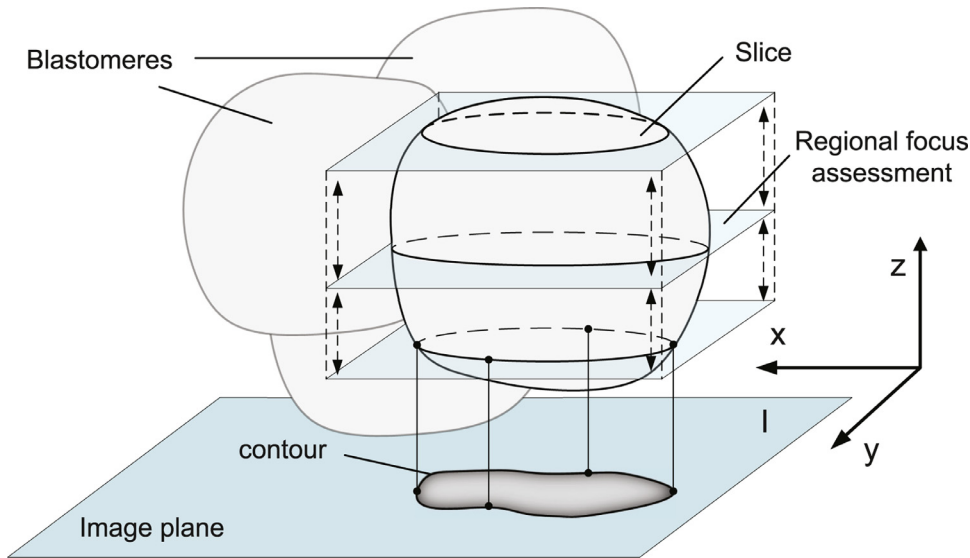


Fig. 6. 3D relocation of individual blastomeres.

the blastomere boundary. The boundary segments that are not detected are then obtained by the machine learning method. A linear regression model with the 10-fold cross-validation [31] is trained using the selected boundary as the training dataset, and the remaining boundary to the outline of blastomeres is estimated using the trained model. For early-stage embryos with more than two blastomeres, boundaries are detected separately. Eventually, the entire boundary estimation is completed, and together with the outline acquired previously, the contours for each blastomere are obtained on the in-focus optical section.

2.5. 3D Relocalization and modeling for individual blastomeres

In this step, individual blastomeres are located and modeled in 3D by extracting the contours of each blastomere in all optical sections of the z-stack image, as illustrated in Fig. 6. Note that other image optical sections also contain the slices of each blastomere that are in focus, but the effect of out-of-focus features appear due to the slice projection from upper or lower sections. For 3D modeling, the contours from such defocused optical sections are required.

Based on the contours obtained previously, the most in-focus sections for each blastomere are relocated by a regional focus measurement, which uses the focus measure operator in Section 2.2 but limits the assessment regions within the contours of individual blastomeres. Then, the coarse-to-fine procedure in Section 2.3 is conducted for individual blastomeres. The most in-focus section of specific blastomere always has the largest area of the corresponding blastomere among all its slices in the z-stack. After individual blastomeres are identified on its focus section, its contour is unitized as the initialization in the localized region-based active contour algorithm for locating other slices of the blastomere in the upper and lower sections. Note that along the z axis direction, the segmentation result in each optical section is then used as the initialization for the active contour model in the next section, until the tip of each blastomere is encountered in an image, hence no additional area is detected and the algorithm stops. Accordingly, all slices of individual blastomeres are obtained in the z-stack by this method.

Following by the centroid calculation of all slices in the z-stack, the 3D position of individual blastomeres can be located. Using a weighted average method, the blastomere coordinate $\bar{B}(\bar{x}, \bar{y}, \bar{z})$ is acquired as

$$\begin{cases} \bar{x} = \frac{1}{N} \sum_{i=1}^N x_i \\ \bar{y} = \frac{1}{N} \sum_{i=1}^N y_i \\ \bar{z} = \frac{\sum_{i=1}^N (S_i \cdot z_i)}{\sum_{i=1}^N S_i} \end{cases} \quad (11)$$

where i denotes the index of optical sections, N represents the total number of slices for individual blastomeres, $B_i(x_i, y_i, z_i)$ and S_i are the centroid coordinate and area of the blastomere for corresponding section, respectively.

3D model of blastomeres is also reconstructed according to all the contours extracted from the z-stack images. Two techniques, namely surface rendering and volume rendering, are mainly used to visualize the 3D structure from the sampled data [32]. While the surface rendering approach requires a great amount of geometric primitives for the surface estimation and often loses considerable information contained within the z-stack images, volume rendering method can convey more information and allow us to fully reveal the internal structure of 3D data to be fully revealed. Volume rendering also exhibits the advantages of high reconstruction accuracy without intermediate surface extraction steps, as mentioned in [8]. Thus, 3D reconstruction of blastomeres is accomplished with good resolution using volume rendering, thereby 3D information of blastomeres is provided for successive PGD operations.

3. Experiments and results

Experiments were performed to validate the practicability and reliability of the proposed method. As displayed in Fig. 7, a standard bright-field inverted microscope platform (Nikon Ti-U) with a robotic micro-manipulator (Scientifica Patchstar) was developed. The $40\times$ Objective lens (CFI Achrom LWD NAMC 40XC) was selected, and illuminator (Prior Scientific LDB103NI) provided standard brightfield illumination for the experiments. Concretely, controlled by the motion controller (ProScan III), the 2-degree-of-freedom precision motorized stage (Prior Scientific H117) carried the petri dish, where the embryos were held. Mouse embryos at the early stage were used in the experiments with the approval from the University of Toronto Health Sciences Research Ethics Board, since they share similar analogs with human embryos. Focus Motor (Prior Scientific PS3H122R), which can provide step sizes as small as $0.002\mu\text{m}$, gave excellent resolution for precise and repeatable focussing in the z axis. Images were captured by the high performance CMOS camera (QImaging optiMOS) with a high resolution of 1920×1080 and a corresponding pixel density $6.23 \text{ pixel}/\mu\text{m}$, and then sent to the desktop computer (Intel(R) Core(TM) i7-3770, CPU 3.40 GHz, RAM 16 GB) for further processing. All algorithms were implemented in Mathworks MATLAB.

Based on the experimental setup, the DOF of the microscope was firstly calculated as $2.41 \mu\text{m}$ using Eq. (1), which means the focal size Δz should be lower than the DOF value. Therefore, 50 images of 2-cell stage mouse embryo with the interval of $2 \mu\text{m}$ were captured to

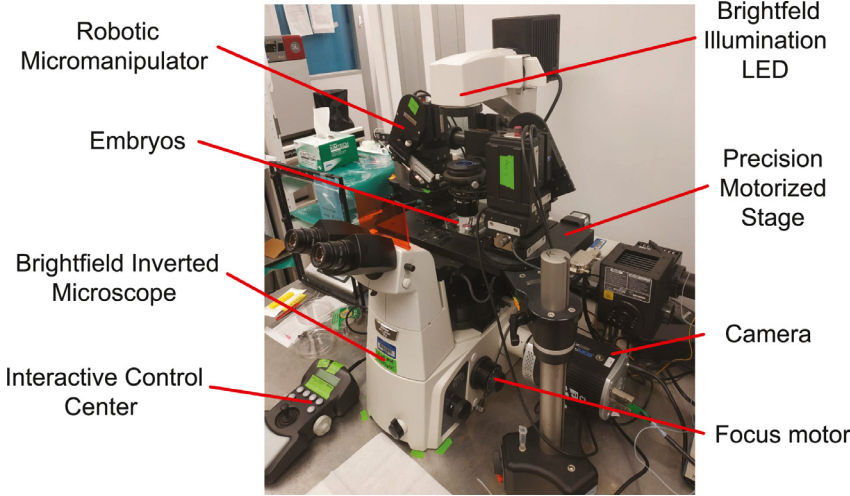


Fig. 7. The experimental setup: robotic brightfield microscopy system.

Table 1
Parameters of PSF for deconvolution.

| Name | Value |
|---|---------------------------------|
| numerical aperture of the microscope (NA) | 0.55 |
| wavelength (λ) | 550 μm |
| magnification factor (M) | 40 |
| refractive index of the lens immersion medium | 1 |
| refractive index of specimen | 1.35 |
| refractive index of coverslip | 1.50 |
| dimension | 675 \times 675 \times 50 |

create the z-stack. The global focus assessment of the z-stack images was then conducted based on Tenengrad variance operator, and the most in-focus section of the embryo was confirmed as the 18th section of the z-stack. Using Gabor filters in Eq. (3), the embryo location in the field of view were automatically obtained, and a region of interest was selected with size 675 \times 675 \times 50 pixels. For original data size 1920 \times 1080 \times 50 pixels, locating the most in-focus embryo in the full-resolution z-stack image took 88.01 seconds. In terms of the parameters of the objective lens and the illuminator as listed in Table 1, the 3D PSF was constructed, and the deconvolution was completed in the region of interest of the z-stack using the RLTV method in Eq. (5). 30.64 seconds were consumed for the 3D PSF construction and the deconvolution process. Then, the coarse-to-fine method was used to identify the blastomeres inside the embryo, which cost 11.87 seconds in total.

After the blastomere outline was segmented from the embryo, the boundary between individual blastomeres was detected using the *a contrario* model given in Eq. (7). Then, using the detected boundary coordinates as the training set, a learning-based model was built and the remaining boundary segments were estimated by linear regression. The entire boundary estimation cost 5.48 seconds. Once the contours for each blastomere were acquired on the embryo focus section, the regional focus assessment was conducted in the z-stack for each blastomere separately, and the blastomere focus sections were relocated as 18th and 19th sections, respectively. After the contours of individual blastomeres were refined by the proposed coarse-to-fine method on their focus sections, the localized region-based active contour was used again to further extract the contours in defocus sections for each blastomere, and the initializations for the active contour model were continuously updated using the segmentation result in the prior section. On average, it took 6.45 seconds to extract each slice in an image. As presented in Fig. 8(a) and 8(b), all slices of the blastomeres in the z-stack were eventually obtained as the first blastomere located between 4th and 34th sections, the second blastomere located between

and 30th sections. The area and centroid of each blastomere in different sections of the z-stack were simultaneously calculated. According to Eq. (11) and the pixel density, the blastomere coordinates were located as $\bar{B}^{(1)}$ (160.337, 71.007, 38.008 μm) and $\bar{B}^{(2)}$ (151.515, 105.860, 36.083 μm). The 3D reconstruction of blastomeres was then achieved using the visualization framework [33], as exhibited in Fig. 8(c).

4-cell mouse embryos were also used to verify the robustness of the proposed method. Focus assessments were conducted for multiple times to separately estimate the boundaries between each blastomere pair, and all blastomeres were then successfully segmented and reconstructed following the same pipeline. As shown in Fig. 8(d), all four blastomeres inside the embryo were reconstructed, which indicates the proposed method is also capable of 3D imaging for 4-cell embryos.

Overall, the computation time of the entire procedure was around 6 minutes under the current experimental setup. Decreasing camera resolution and image sizes will contribute to reducing the time cost. Moreover, with the development of the computer hardware, utilization of the multi-core GPU, conduction of parallel processing procedures, conversion from MATLAB to a more efficient programming language such as C/C++, the time cost can be significantly reduced.

To evaluate the proposed method, the blastomeres have been manually segmented in each section of the z-stack with the pixel-wise annotation by Image Processing and Computer Vision Toolbox from MATLAB. After the annotation, the pixel coordinates of the manually recognized boundaries (MB) were recorded, and then were compared to the automatic segmented boundaries (AB) from the proposed method. A PrecisionScore is applied to estimate the precision of the proposed method, which is defined as

$$\text{PrecisionScore} = \frac{n(AB \psi MB)}{n(AB)} \quad (12)$$

where $n(AB)$ is the number of pixels of AB for each section, $n(AB \psi MB)$ is the number of the true results. $AB \psi MB$ is defined as the true when MB intersects with a 3-pixel neighborhood of AS. As presented in Fig. 9(a), the green squares denote AB pixels, the red squares denote MB pixel, and the yellow squares denote the neighborhood pixels of AB, and the blue boundary gives an example of the neighborhood of a target AB pixel. If the blue boundary includes a MB pixel, the target AB pixel is deemed as precise, and $AB \psi MB$ is true. If the PrecisionScore reaches 85% or higher, the automatic segmentation is regarded as accurate and successful. As illustrated in Fig. 9(b), out of 31 blastomere images in the z-stack, the AB of 28 images were correctly segmented, and the precision rate is 90.32%. The coordinates of the manual recognized blastomere were also obtained as $\bar{B}_m^{(1)}$ (160.151, 71.167, 38.014 μm). The distance between $\bar{B}^{(1)}$ and $\bar{B}_m^{(1)}$ is 1.028 μm , which proves that the proposed method is very close to human visual perception.

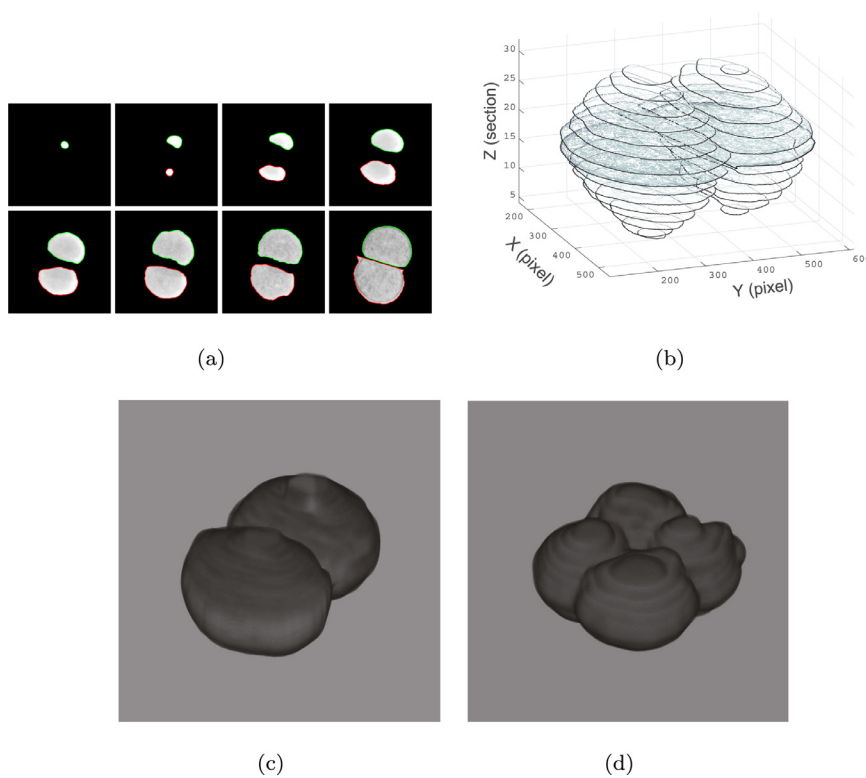


Fig. 8. Experimental results on the early-stage embryos. (a) Blastomere contour extraction on Section 4, 6, 8, 10, 12, 14, 16, 18. (b) Distribution of blastomere slices along z-axis. (c) Blastomeres in 2-cell embryo. (d) Blastomeres in 4-cell embryos.

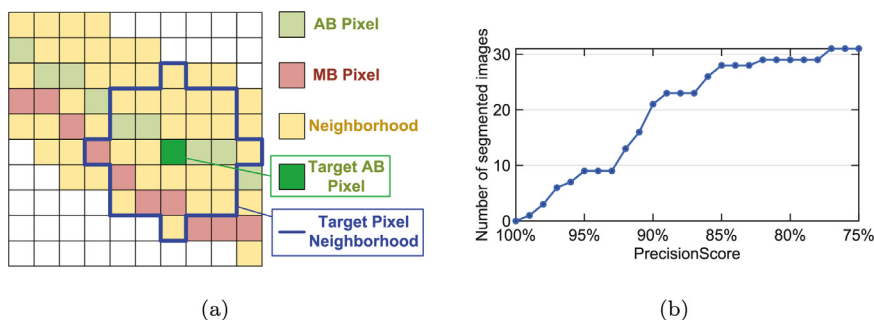


Fig. 9. Comparisons with manual annotations. (a) Diagram of $AB\psi MB$. (b) PrecisionScore.

4. Conclusions

This study develops a 3D imaging technique to automatically identify and locate blastomeres inside early-stage embryos for PGD under brightfield microscopy. A guideline of z-stack image acquisition is firstly proposed, and focus assessment and Gabor filters are employed to locate the most in-focus optical section of the embryo and its position in the field of view. After the RLTV deconvolution for the region of interest in the z-stack, a coarse-to-fine method that combines localized region-based active contour and subpixel edge locating algorithms are used to identify the outline of blastomeres inside the embryo. Then, a boundary estimation method is presented based on *A contrario* model and linear regression. Following by the blastomere contour extraction in the z-stack, the 3D coordinates of individual blastomeres are obtained, and 3D reconstruction is achieved by volume rendering.

The experiments are performed on 2-cell and 4-cell mouse embryos, and the results demonstrate that the proposed technique is effective and accurate for 3D blastomere identification inside embryos based on conventional brightfield microscopy, thereby allowing multiple dimensional embryo manipulation under the robotic systems, such as reposition and reorientation of the embryo. This 3D imaging technique also

provides blastomere distributions and visualization inside the embryo, which is useful for embryo analysis and enables the global optimum of desired location for biopsy to be found.

Our method not only provides a good candidate for the 3D visualization of blastomeres in automated PGD using conventional tools that smaller laboratories can afford, but also a starting point in embryo biopsy prior to subsequent automation procedures such as embryo position and orientation control, zona breaching, and blastomere extraction. In future studies, the global optimization of dissection position selection and visual servo strategy for automatic embryo biopsy under the robotic brightfield microscopy system will be investigated.

Declaration of Competing Interest

We declare that we have no financial and personal relationships with other people or organizations that can inappropriately influence our work, there is no professional or other personal interest of any nature or kind in any product, service and/or company that could be construed as influencing the position presented in, or the review of, the manuscript entitled, Automatic three-dimensional imaging for blastomere identification in early-stage embryos based on brightfield microscopy.

CRediT authorship contribution statement

Sheng Yao: Writing - original draft, Methodology, Software.
James K. Mills: Conceptualization, Supervision. **Ihab Abu Ajamieh:** Resources. **Hai Li:** Writing - review & editing. **Xianmin Zhang:** Funding acquisition, Supervision.

Acknowledgments

This work was supported by the **National Natural Science Foundation of China (NSFC) (51820105007, U1609206, 51905176)**. The authors would also like to thank the financial support from **China Scholarships Council (CSC) (201806150058)** for research in **University of Toronto**.

References

- [1] Abu Ajamieh I, Benhabib B, Mills JK. Automatic system for the blastocyst embryo manipulation and rotation. *Ann Biomed Eng* 2019. doi:10.1007/s10439-019-02360-8.
- [2] Braude P, Pickering S, Flinter F, Ogilvie CM. Preimplantation genetic diagnosis. *Nat Rev Genet* 2002;3(12):941.
- [3] Won SY, Kim H, Lee WS, Kim JW, Shim SH. Pre-implantation genetic diagnosis and pre-implantation genetic screening: two years experience at a single center. *Obstetrics & gynecology science* 2018;61(1):95–101.
- [4] Zhang Z, Liu J, Wang X, Zhao Q, Zhou C, Tan M, et al. Robotic pick-and-place of multiple embryos for vitrification. *IEEE Rob Autom Lett* 2016;2(2):570–6.
- [5] Wong CY, Mills JK. Automation and optimization of multipulse laser zona drilling of mouse embryos during embryo biopsy. *IEEE Trans Biomed Eng* 2016;64(3):629–36.
- [6] Wang Z, Ang WT. Automatic dissection position selection for cleavage-stage embryo biopsy. *IEEE Trans Biomed Eng* 2015;63(3):563–70.
- [7] Shakoor A, Xie M, Luo T, Hou J, Shen Y, Mills JK, et al. Achieving automated organelle biopsy on small single cells using a cell surgery robotic system. *IEEE Trans Biomed Eng* 2018;66(8):2210–22.
- [8] Gao W, Shakoor A, Zhao L, Jiang Z, Sun D. 3-D image reconstruction of biological organelles with a robot-aided microscopy system for intracellular surgery. *IEEE Rob Autom Lett* 2018;4(2):231–8.
- [9] Sooriyaeevan JM. Applications of optical principles in clinical x-ray visualization. *Opt Lasers Eng* 2014;54:197–202.
- [10] Cao B, Kelbauskas L, Chan S, Shetty RM, Smith D, Meldrum DR. Rotation of single live mammalian cells using dynamic holographic optical tweezers. *Opt Lasers Eng* 2017;92:70–5.
- [11] Sun Y, Nelson BJ. Biological cell injection using an autonomous microrobotic system. *Int J Rob Res* 2002;21(10–11):861–8.
- [12] Rodríguez A, Clemente P, Tajahuerce E, Lancis J. Dual-mode optical microscope based on single-pixel imaging. *Opt Lasers Eng* 2016;82:87–94.
- [13] Degerman J, Winterfors E, Fajjerson J, Gustavsson T. A computational 3d model for reconstruction of neural stem cells in bright-field time-lapse microscopy. In: *Computational Imaging V*, 6498. International Society for Optics and Photonics; 2007. p. 64981E.
- [14] Sadanandan SK, Ranefall P, Le Guyader S, Wählby C. Automated training of deep convolutional neural networks for cell segmentation. *Sci Rep* 2017;7(1):7860.
- [15] Giusti A, Corani G, Gambardella L, Magli C, Gianaroli L. Blastomere segmentation and 3d morphology measurements of early embryos from hoffman modulation contrast image stacks. In: *2010 IEEE International Symposium on Biomedical Imaging: From Nano to Macro*. IEEE; 2010. p. 1261–4.
- [16] Giusti A, Taddei P, Corani G, Gambardella L, Magli C, Gianaroli L. Artificial defocus for displaying markers in microscopy z-stacks. *IEEE Trans Vis Comput Graph* 2011;17(12):1757–64.
- [17] Jennings PC, Merriman JA, Beckett EL, Hansbro PM, Jones KT. Increased zona pellucida thickness and meiotic spindle disruption in oocytes from cigarette smoking mice. *Human reproduction* 2011;26(4):878–84.
- [18] Osibote O, Dendere R, Krishnan S, Douglas T. Automated focusing in bright-field microscopy for tuberculosis detection. *J Microsc* 2010;240(2):155–63.
- [19] Pech-Pacheco JL, Cristóbal G, Chamorro-Martinez J, Fernández-Valdivia J. Diatom autofocusing in brightfield microscopy: a comparative study. In: *Proceedings 15th International Conference on Pattern Recognition. ICPR-2000*, 3. IEEE; 2000. p. 314–17.
- [20] Pertuz S, Puig D, Garcia MA. Analysis of focus measure operators for shape-from-focus. *Pattern Recognit* 2013;46(5):1415–32.
- [21] Jain AK, Farrokhnia F. Unsupervised texture segmentation using gabor filters. *Pattern Recognit* 1991;24(12):1167–86.
- [22] Jolliffe I. *Principal component analysis*. Springer; 2011.
- [23] Otsu N. A threshold selection method from gray-level histograms. *IEEE Trans Syst Man Cybern* 1979;9(1):62–6.
- [24] Dey N, Blanc-Feraud L, Zimmer C, Roux P, Kam Z, Olivo-Marin J-C, et al. Richardson-lucy algorithm with total variation regularization for 3d confocal microscope deconvolution. *Microsc Res Tech* 2006;69(4):260–6.
- [25] Li J, Xue F, Blu T. Fast and accurate three-dimensional point spread function computation for fluorescence microscopy. *JOSA A* 2017;34(6):1029–34.
- [26] Chan TF, Vese LA. Active contours without edges. *IEEE Trans Image Process* 2001;10(2):266–77.
- [27] Lankton S, Tannenbaum A. Localizing region-based active contours. *IEEE Trans Image Process* 2008;17(11):2029–39.
- [28] Trujillo-Pino A, Krissian K, Alemán-Flores M, Santana-Cedrés D. Accurate subpixel edge location based on partial area effect. *Image Vis Comput* 2013;31(1):72–90.
- [29] Lezama J, Morel J-M, Randall G, Von Gioi RG. A contrario 2d point alignment detection. *IEEE Trans Pattern Anal Mach Intell* 2014;37(3):499–512.
- [30] Von Gioi RG, Jakubowicz J, Morel J-M, Randall G. Lsd: a fast line segment detector with a false detection control. *IEEE Trans Pattern Anal Mach Intell* 2010;32(4):722–32.
- [31] Bishop CM. *Pattern recognition and machine learning*. springer; 2006.
- [32] Kaufman A, Mueller K. Overview of volume rendering. *The visualization handbook* 2005;7:127–74.
- [33] Schmid B, Schindelin J, Cardona A, Longair M, Heisenberg M. Software a high-level 3d visualization api for java and imagej; 2010.
- [34] Li H, Zhang XM, Zhu BL, Wei JY, Fatikow S. Pose sensing and servo control of the compliant nanopositioners based on microscopic vision. *IEEE Trans Ind Electron* 2020. doi:10.1109/TIE.2020.2977572.